
White Rose Research Online

eprints@whiterose.ac.uk
https://eprints.whiterose.ac.uk
Universities of Leeds, Sheffield and York

Deposited via The University of Sheffield.

White Rose Research Online URL for this paper:
https://eprints.whiterose.ac.uk/id/eprint/245869/

Version: Accepted Version

Article:
Wong, H.Y.L., Sullivan, A.L. and Zhang, Y. (2026) Machine-learning-enabled three-dimensional firebrand transport characterisation: combustion enhancement, morphology and rotational dynamics. Proceedings of the Combustion Institute, 42. 106433. ISSN: 1540-7489

https://doi.org/10.1016/j.proci.2026.106433

© 2026 The Authors. Except as otherwise noted, this author-accepted version of a journal article published in Proceedings of the Combustion Institute is made available via the University of Sheffield Research Publications and Copyright Policy under the terms of the Creative Commons Attribution 4.0 International License (CC-BY 4.0), which permits unrestricted use, distribution and reproduction in any medium, provided the original work is properly cited. To view a copy of this licence, visit http://creativecommons.org/licenses/by/4.0/

Reuse
This article is distributed under the terms of the Creative Commons Attribution (CC BY) licence. This licence allows you to distribute, remix, tweak, and build upon the work, even commercially, as long as you credit the authors for the original work. More information and the full terms of the licence here: https://creativecommons.org/licenses/

Takedown
If you consider content in White Rose Research Online to be in breach of UK law, please notify us by emailing eprints@whiterose.ac.uk including the URL of the record and the reason for the withdrawal request.





Machine-Learning-Enabled Three-Dimensional Firebrand Transport Characterisation: Combustion Enhancement, Morphology and Rotational Dynamics

Hugo Yu Lam Wong[a,*], Andrew L. Sullivan[b], Yang Zhang[a,*]

[a] *School of Mechanical, Aerospace and Civil Engineering, The University of Sheffield, Sheffield S1 3JD, United Kingdom*
[b] *Commonwealth Scientific and Industrial Research Organisation, Canberra, Australia*

Abstract

Firebrand spotting, responsible for 30–60% of structure ignitions in wildland–urban interface zones, has historically been constrained by slow, inter-operator-variable manual tracking. This work introduces an integrated stereo-vision and YOLOv8n-seg framework for automated three-dimensional firebrand transport quantification. The automated framework processes over 250,000 frames at 70 fps (≈2800× speedup), achieves 95.9% mean average precision (mAP), and reduces per-trajectory analysis from 5–10 h of operator time to under 10 min. Position uncertainty is ±2.1 mm and velocity uncertainty ±0.15 m s^{-1}. The 108-experiment factorial dataset reveals that vortical flow modification increases path-integrated transport distance by ≈41% over the quiescent control, with active combustion adding a further ≈2% through effective buoyancy enhancement (F_{buoy} = 1.15–1.24) and mass loss. Maximum transport heights rise by 9.96% under combined burning + vortex relative to vortex-only. Rotation-frequency and orientation-persistence statistics are consistent with rotation-mediated stabilisation for open-shaped firebrands, although passive aerodynamic alignment cannot be excluded with the present measurements. Morphology-specific drag coefficients (0.68–1.47) and effective buoyancy enhancement factors (1.15–1.24) provide laboratory-derived parameters for future wildfire spotting model development.

Novelty and significance statement

An integrated automated stereo-tracking framework combining YOLOv8n-seg instance segmentation with stereo vision yields simultaneous position, orientation and morphometric data at every time step. The resulting 108-experiment factorial dataset—infeasible with manual digitisation—disaggregates transport enhancement into dominant vortex-driven and modest combustion-driven components, and supplies evidence consistent with rotation-mediated stabilisation and distinguishes beneficial orientation persistence from destabilising high-frequency tumbling across bark morphologies. Morphology-specific drag coefficients (0.68–1.47) and effective buoyancy enhancement factors (1.15–1.24) address a recognised gap where generic spherical-particle assumptions persist despite the aerodynamic complexity of natural firebrands. The methodology demonstrates that ML-enabled combustion diagnostics resolves physical relationships undetectable at conventional sample sizes.

Keywords: Firebrand transport; Machine learning; YOLOv8n-seg; Wildfire dynamics; Combustion enhancement

*Corresponding author.

1. Introduction

Wildfire spotting through firebrand transport is a primary mechanism by which fires breach containment, with documented transport distances exceeding 40 km [1,2]. The 2019–2020 Australian bushfires burned 18.6 million hectares and destroyed 5,900 structures, and California's 2020 fires incurred over $2.1 billion in suppression costs. Firebrands generated from bark, leaves and woody debris are lofted in the turbulent plume above a fire front, transported downwind, and deposited onto receptive fuels, where they may initiate new ignitions well ahead of the flaming front [6,10].

Foundational work by Tarifa et al. [3] established the terminal-velocity framework for burning wooden particles, and subsequent studies characterised the aerodynamic behaviour of naturally generated bark firebrands [4,5]. Wind-tunnel experiments with rod- and disk-shaped model firebrands have quantified drag coefficients and trajectory statistics for idealised shapes [8,19,23]. Field and semi-field experiments with firebrand generators [7,25,26] have shown that firebrand showers span broad size and mass distributions and are strongly influenced by fire-induced flow structures. Numerical studies [17,18,21,22] have further shown that the fire-plume updraft, rather than self-induced buoyancy of individual firebrands, is typically the dominant driver of lofting height. Despite these advances, quantitative three-dimensional transport data for naturally generated firebrands remain limited by: (1) low experimental throughput and inter-operator variability exceeding 30% in manual trajectory digitisation [5,10]; (2) sparse data on how active combustion modulates transport beyond the terminal-velocity effect of progressive mass loss; (3) undefined

morphology–performance links for firebrands with complex, non-idealised shapes [4,5]. These constraints have restricted most investigations to fewer than 100 individual firebrand trajectories [8,10], which is insufficient to resolve morphology-specific behaviour with statistical confidence.

The present study performs automated single-firebrand three-dimensional tracking in the CSIRO vertical wind tunnel (VWT) for three eucalyptus bark morphologies under quiescent, vortical, and burning-with-vortical flow conditions. To make the full 108-experiment factorial design tractable, the analysis pipeline replaces manual frame-by-frame digitisation with a deep-learning-based detection and segmentation stage. Existing ML-based fire applications have largely focused on binary classification such as flame-presence detection; quantitative instance segmentation of individual firebrands has only recently emerged [13,27]. The YOLOv8n-seg architecture was selected because its single-stage design and per-instance segmentation masks provide position, orientation and projected area at every time step, with inference throughput exceeding the stereo acquisition rate so that all frames are processed without subsampling. Building on the 3D particle tracking of Bouvet et al. [13] and the multi-view methodology of Abdelaziz and Sullivan [27], the present work integrates instance segmentation with stereo reconstruction to yield concurrent position, orientation and morphometric data.

The specific objectives are to: (1) develop and validate an automated 3D single-firebrand tracking pipeline; (2) quantify the contribution of active combustion to transport over a controlled factorial matrix; (3) derive morphology-dependent drag coefficients for naturally shaped eucalyptus bark firebrands; (4) analyse rotational dynamics and examine whether orientation statistics are consistent with a gyroscopic stabilisation mechanism; (5) provide empirical parameters for wildfire spotting models. The investigation focuses on *Eucalyptus mannifera* bark, which represents a significant spotting hazard in Australian fire regimes [4,5].

2. Experimental Methodology

2.1. Facility and sample preparation

Experiments were conducted in the CSIRO vertical wind tunnel [14,15]. The VWT has a 77 × 77 cm cross-section and a 425 cm diverging working section with uniform upward flow (0.1–20.0 m s^{-1}, ±1% velocity precision). Turbulence intensity in the central test region is below 0.6% [15], and the divergent taper allows firebrands to equilibrate within a velocity gradient. A custom vortex generator with eight helical blades (35° pitch angle) produced tangential velocities of 1.4–2.8 m s^{-1} superimposed on axial velocities of 2.0–4.0 m s^{-1}, validated by pitot-static mapping (±5% agreement with CFD predictions).

The previously cited VWT studies [14,15,27] did not incorporate a vortical impeller. The generator here was not intended to reproduce a complete wildfire plume; it provided a repeatable laboratory-scale means of introducing a controlled tangential velocity component and rotational flow structure, allowing the separate influence of structured vortical motion on firebrand trajectories to be examined. Detailed turbulence statistics downstream of the insert were unavailable in the present study and are acknowledged as a limitation. A CAD (STL) geometry of the impeller is provided as supplementary material to enable numerical replication. Fig. 1 shows the VWT working section, camera positions and impeller.

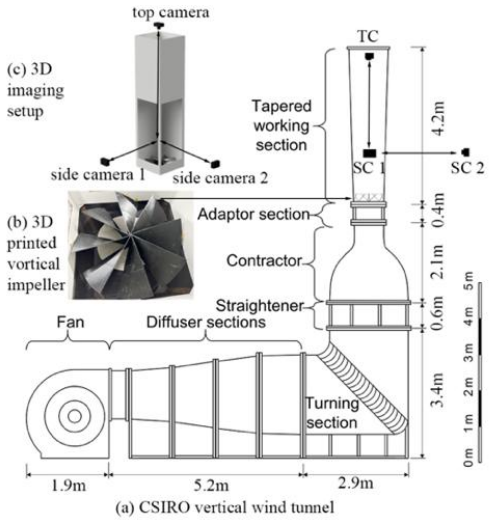


Fig. 1. (a) Schematic of the CSIRO VWT working section. (b) 3D-printed helical vortex-generator insert (eight blades, 35° pitch). (c) Cut-away view with stereo-camera positions and firebrand release point.

Seven bark morphologies observed on mature *Eucalyptus mannifera* trees at the CSIRO site are grouped into three aerodynamically distinct classes—Open, Semi-open and Closed—by the chord-to-arc length ratio defined below. Because the Recurved and Channelled sub-types are difficult to distinguish in the original photographic panel, Fig. 2 adds annotated side-profile schematics for each sub-type.

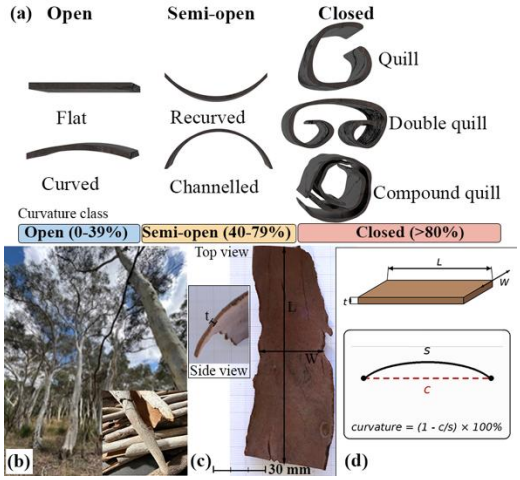


Fig. 2. Eucalypt bark morphology and the dimensional conventions used in this study. **(a)** Seven representative bark sub-types grouped into three curvature classes according to the chord-to-arc ratio c/s: *Open* (0–39 %) — Flat, Curved; *Semi-open* (40–79 %) — Recurved, Channelled; and *Closed* (> 80 %) — Quill, Double quill, Compound quill. **(b)** Source eucalypt forest (*Eucalyptus* spp.) and the bark substrate harvested for specimen preparation. **(c)** Representative bark specimen showing the top view with longitudinal length L and tangential width W, and an inset side view showing the radial thickness t; scale bar 30 mm. **(d)** Isometric schematic of a bark plate defining L, W and t (upper), together with the cross-sectional curvature geometry (lower), in which the chord c connects the endpoints of the arc s and curvature is defined as $(1 - c/s) \times 100$ %. Each sub-type in (a) is assigned to its class on the basis of this metric.

Sample preparation comprised digital photography, dimensional measurement (±0.01 mm) and oven drying at 105 °C for 24 h to constant mass (±0.001 g). All dimensional and mass measurements were performed after drying to avoid systematic bias from post-drying shrinkage observed in pilot measurements on eucalypt bark. Morphological classification used the chord-to-arc length ratio: Open (0–39% curvature, 60–120 × 15–45 × 1–3 mm); Semi-open (40–79%, 55–100 × 12–35 × 2–5 mm); Closed (>80%, 45–90 × 8–25 × 3–8 mm), consistent with Ellis [4].

The principal moment of inertia I about the spin axis (the longitudinal axis passing through the centre of mass, about which steady-state rotation was observed in preliminary trials) was computed from a 3D reconstruction of each dried sample: samples were 3D-scanned and photographed, and the inertia tensor was obtained by volumetric integration assuming uniform density with total mass constrained by the measured dry weight. I corresponds to the smallest eigenvalue of the tensor, consistent with the observed spin axis. Uncertainty from scan resolution and the uniform-density assumption was estimated at ±12% per sample and propagated into the reported inter-sample standard deviations. Mean values are $I = 2.41 \pm 0.64 \times 10^{-6}$ kg m^2 (Open), $3.10 \pm 0.89 \times 10^{-6}$ kg m^2 (Semi-open) and $4.04 \pm 1.12 \times 10^{-6}$ kg m^2 (Closed).

2.2. Machine learning detection and 3D trajectory reconstruction

The tracking framework combines YOLOv8n-seg instance segmentation [11,12] with stereo vision for three-dimensional trajectory reconstruction. YOLOv8n-seg was selected from three candidates: Mask R-CNN reached 94.1% mAP at only 12 fps; YOLOv8s-seg reached 96.2% mAP at 45 fps with substantially higher computational cost; the nano-variant (3.2 M parameters, 8.7 GFLOPs) delivered 95.9% mAP@0.5 at 70 fps—the only candidate exceeding the 50 fps camera rate while maintaining >95% accuracy. Mean average precision (mAP) is the mean of per-class average precision at an intersection-over-union (IoU) threshold of 0.5, where IoU is the ratio of intersection to union of the predicted and ground-truth segmentation masks. The pipeline is capable of processing at rates exceeding the acquisition frame rate on the tested hardware; in the present study the analysis was performed as automated post-processing rather than coupled live acquisition-and-processing. Processing all 250,000+ acquired frames offline without temporal subsampling preserves the temporal resolution needed for rotation-frequency analysis and drag-coefficient estimation.

The model was trained on 9,965 annotated images (70/20/10% train/validation/test) labelled by three expert annotators (mean pairwise Cohen's $\kappa = 0.89$). Of these, 2,486 were original annotated frames and 7,479 were generated by domain-specific augmentation; originals and augmented subsets were balanced across non-burning/burning classes and vortex-off/on flow states. Augmentations fell into three categories: geometric (rotation ±90° and shear ±12°/±13° for orientation invariance), exposure (−8% to +8% for dynamic-range robustness) and noise injection (1.09% of pixels substituted with Gaussian noise for smoke and ember obscuration). Extreme augmentations that could corrupt physically meaningful features—large colour shifts distorting flame boundaries, motion blur exceeding the native camera response, or crops removing the firebrand—were deliberately avoided. Representative base and augmented images are provided as supplementary material.

Stereo depth estimation used two synchronised HD cameras with epipolar-geometry constraints and semi-global block matching with sub-pixel interpolation. Pre-experiment calibration following Zhang's method [16] achieved reprojection errors below 0.5 pixels, validated against a known-size reference object. Fig. 3 illustrates representative YOLOv8n-seg segmentation of a rotating firebrand.

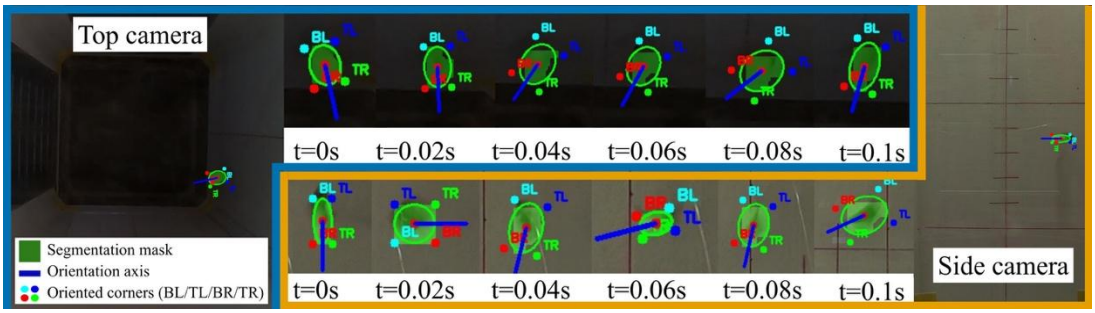


Fig. 3. YOLOv8n-seg tracking of a single *E. mannifera* firebrand over 0.1 s. Left and right panels show the original top- and side-camera views of the in-duct scene at native zoom. Centre: six magnified frames per camera (t = 0–0.1 s) of the detected object from the top (blue frame) and side (orange frame) cameras, with segmentation mask, orientation axis, and four oriented corners (mean IoU = 0.96).

2.3. Experimental protocol and uncertainty analysis

Samples were positioned at the tunnel centreline, 70 cm above the vortex generator. For combustion tests, butane-torch ignition (5 s application, 5 s stabilisation) preceded release, ensuring repeatable ember penetration. Data acquisition began 2 s before release and continued until the sample exited the field of view or burnt out. Environmental logging at 1 Hz recorded temperature (±0.1 °C), humidity (±1%) and pressure (±0.1 mbar).

The full test matrix comprised 3 morphologies × 3 flow conditions × 12 replicates = 108 experiments. The three flow conditions are defined in Table 1. The pipeline's throughput of 25–30 experiments per week, versus 5–8 per week by manual digitisation (three views × ~1,000 frames × 4 bounding-box corners ≈ 12,000 picks per trajectory, 5–10 h of operator time, consistent with the manual components of [13,27]), made the factorial tractable. A burning-only (no-vortex) cell was deliberately omitted: the control and vortex-only cases isolate the aerodynamic contribution without combustion, and the burning + vortex case adds the combustion contribution on top. Of the 108 designed trajectories, 24 were excluded — primarily due to in-flight sample fragmentation during combustion, with a smaller number of tracking failures — leaving 84 retained trajectories for analysis (control n = 30, vortex-only n = 24, burning + vortex n = 30).

Table 1. Definition of the three flow conditions; n = 12 replicates per morphology (Open, Semi-open, Closed) per condition.

Condition	Axial	Tangential	Combustion
A—Control	Quiescent	None	Non-burning
B—Vortex-only	2.0–4.0 m s^{-1}	1.4–2.8 m s^{-1}	Non-burning
C—Burning + vortex	2.0–4.0 m s^{-1}	1.4–2.8 m s^{-1}	Burning (5 s ign. + 5 s stab.)

Post-processing included lens-distortion correction, YOLOv8n-seg inference, feature-based stereo matching, direct linear transformation (DLT) for 3D position recovery and Kalman filtering for motion continuity, following principles consistent with recent multi-view firebrand tracking methodologies [27]. Fig. 4 shows a representative 3D-reconstructed trajectory, illustrating the spatial extent of firebrand motion captured by the pipeline.

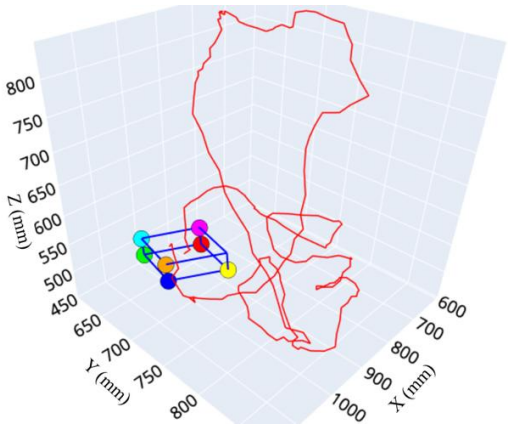


Fig. 4. 3D-reconstructed trajectory of a representative firebrand. Red curve: Kalman-smoothed position; markers: oriented bounding-box corners at selected frames; axis labels: motion span in millimetres.

The uncertainty budget is summarised in Table 2.

Table 2. Summary of measurement and derived-quantity uncertainties. The ± values reported on means in the Results refer to inter-sample standard deviations unless otherwise stated.

Quantity	Uncertainty	Note
3D position	±2.1 mm	RSS of calibration, centroid jitter, temporal averaging, residual distortion

Quantity	Uncertainty	Note
Velocity	±0.15 m s^{-1}	Position-uncertainty propagation over 20 ms interval
Projected area A	±7%	Segmentation-boundary variation inferred from mAP
Terminal velocity v_t	≈22%	Inter-trajectory variance at quasi-steady equilibrium
Drag coeff. C_D (single)	≈±45%	Quadratic dependence on v_t dominates
Mean C_D (n = 12)	≈±13%	Standard error after √12 reduction
Moment of inertia I	±12%	Scan resolution and uniform-density assumption
Detection mAP@0.5	95.2 / 93.8 / 94.1%	Non-burning / active burning / vortex flow; morphology 93.2–95.8%; tracking continuity 96.3%

The drag coefficient was estimated under a quasi-steady force-balance assumption applied during the terminal-velocity phase of each trajectory:

$$C_D = \frac{2(m - m_{disp})\, g}{\rho A v_t^2} \quad (1)$$

where m is mass (corrected for combustion mass loss via pre/post weighing and linear interpolation), m_{disp} the displaced air mass, ρ the air density, A the instantaneous projected area from the segmentation mask (measured from the top view, Fig. 3), and v_t the terminal velocity. The balance is applied only to quasi-steady segments, not during transient phases or rapid orientation changes.

Sensitivity of C_D to segmentation quality was not formally assessed by mask-perturbation testing. The projected-area uncertainty (≈±7%) propagates linearly into C_D, while terminal-velocity uncertainty ($\delta v_t/v_t \approx 22\%$) enters quadratically and dominates: $\delta C_D/C_D = \sqrt{[(\delta A/A)^2 + (2\delta v_t/v_t)^2]}$. For typical $A \approx 900$ mm² and $v_t \approx 0.68$ m s^{-1}, single-measurement C_D uncertainty is ≈±45%, reducing to ≈±13% on the n = 12 mean via √12 averaging.

A net upward thermal buoyancy force F_b reduces the effective gravitational force from mg to $(mg - F_b)$. Under the same force balance, $v_{t,burning}^2 = v_{t,non\text{-}burning}^2 \times (mg - F_b)/mg$ for matched morphology, projected area and drag, so the effective buoyancy enhancement factor is defined as

$$F_{buoy} = \frac{mg}{mg - F_b} = \left(\frac{v_{t,non-burning}}{v_{t,burning}}\right)^2 \quad (2)$$

$F_{buoy} > 1$ corresponds to enhanced effective buoyancy — equivalently, a lower settling velocity for the burning firebrand — and lumps together thermal buoyancy, mass loss, and hot-gas generation under the quasi-steady force-balance assumption. The equivalent fractional upward lift is $F_b/mg = 1 - 1/F_{buoy}$, which for $F_{buoy} = 1.15$–1.24 corresponds to 13–19% of the firebrand weight. Uncertainty is propagated as $\delta F_{buoy}/F_{buoy} = 2\sqrt{[(\delta v_{t,b}/v_{t,b})^2 + (\delta v_{t,nb}/v_{t,nb})^2]}$. Temporal tracking continuity was 96.3%; the 3.7% interpolation fraction was uniformly distributed across morphologies (3.5–3.9%) with interpolation errors below 1.2 px (~3 mm), confirming no morphology-dependent detection bias.

3. Results

3.1. Transport height enhancement

Active combustion enhanced transport heights across all morphologies (Fig. 5). Mean maximum heights were: control (n = 30) 116.5 ± 7.5 cm, vortex-only (n = 24) 117.5 ± 6.8 cm, burning + vortex (n = 30) 129.2 ± 9.8 cm—a 9.96% increase for burning + vortex relative to vortex-only. One-way ANOVA on the 84 retained trajectories confirmed significant differences ($F(8, 75) = 23.47$, $p < 0.001$, $\eta^2 = 0.715$), indicating that condition and morphology collectively explain over 71% of the variance. Post-hoc Tukey HSD identified significant pairwise differences ($p < 0.05$) between combustion and non-combustion conditions for all morphologies.

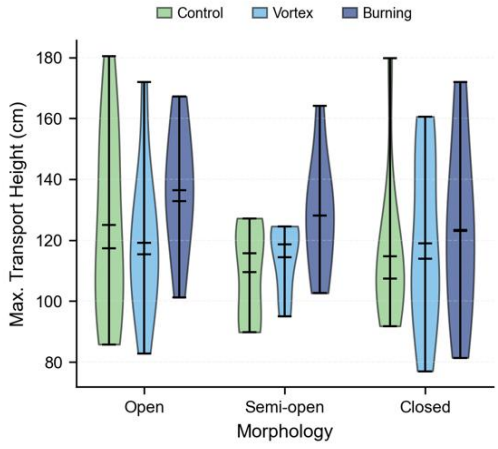


Fig. 5. Maximum transport heights across three morphologies (Open, Semi-open, Closed) and three conditions (Control, Vortex, Burning + Vortex).

Morphology-dependent enhancement varied substantially (Fig. 6): Open firebrands showed the greatest height increase (14.4%: 119.2 → 136.4 cm), followed by semi-open (11.9%: 114.4 → 128.0 cm) and closed (3.4%: 119.0 → 123.0 cm). Open shapes showed slightly reduced heights under vortex-only relative to control (119.2 vs 124.9 cm), suggesting that tangential flow components temporarily

destabilise open-shape flight before rotational effects establish orientation preference.

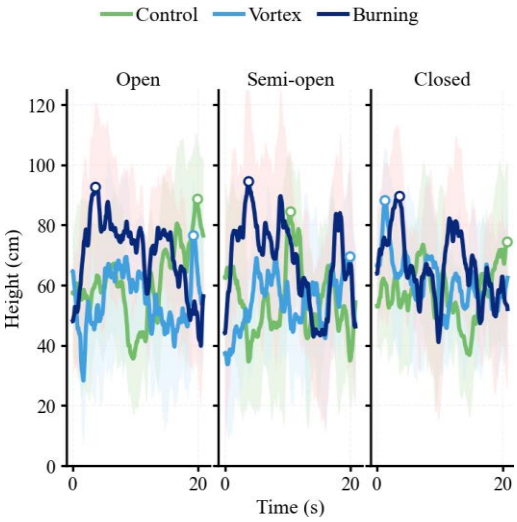


Fig. 6. Condition-averaged transport height vs. time for the three morphologies and three conditions with shaded 95% CI; white circles mark peak mean heights.

3.2. Velocity profiles and path distances

Three-dimensional velocity measurements revealed morphology-dependent vertical transport rates: open 0.68 ± 0.12 m s^{-1}, semi-open 0.71 ± 0.14 m s^{-1}, closed 0.64 ± 0.09 m s^{-1} (ANOVA: $F(2,81) = 14.08$, $p < 0.0001$). Open and semi-open significantly exceeded closed ($p < 0.01$), while open vs semi-open did not differ significantly ($p = 0.275$), suggesting aerodynamic efficiency plateaus for moderately curved geometries. Horizontal r.m.s. velocities rose from 0.15 ± 0.08 m s^{-1} (control) to 0.34 ± 0.16 m s^{-1} (vortex flow); peak horizontal velocities reached 4.2 m s^{-1} for burning open firebrands during descent.

Path-integrated distances over 21 s observation windows (Fig. 7) were 23.42 ± 3.87 m (burning + vortex), 22.94 ± 3.21 m (non-burning vortex) and 16.25 ± 2.43 m (control). Vortex-only flow increased path-integrated distance by 41.2% relative to control (16.25 → 22.94 m); adding combustion increased it by a further 2.1% relative to vortex-only (22.94 → 23.42 m), giving a total increase of 44.1% relative to control. Vortical flow modification is therefore the dominant enhancement mechanism, with combustion adding a smaller but resolvable contribution. Relative to their own control condition, closed shapes showed the greatest proportional increase in path distance under burning + vortex (60%: 14.9 ± 2.2 → 23.8 ± 3.9 m), while open shapes achieved the greatest absolute distances (24.3 ± 4.1 m).

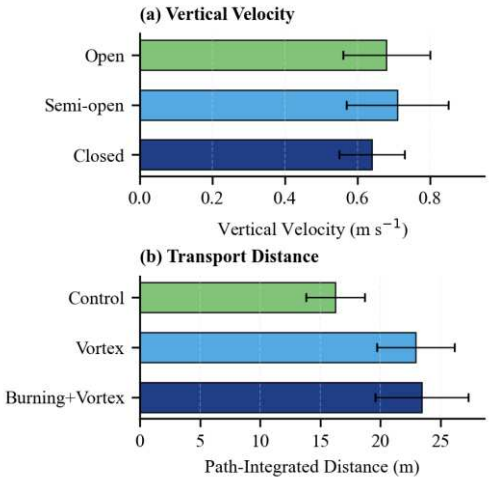


Fig. 7. (a) Mean vertical velocity by morphology (all conditions pooled). (b) Cumulative path-integrated distance by condition, showing both pooled and morphology-specific breakdowns.

3.3. Combustion characterisation

Burning duration varied inversely with geometric enclosure: open 12.4 ± 3.2 s, semi-open 9.7 ± 2.8 s, closed 7.1 ± 2.1 s. Mass-loss rates (open 0.041 ± 0.008, semi-open 0.053 ± 0.012, closed 0.067 ± 0.015 g s^{-1}) inversely correlated with total mass consumption (42 ± 11%, 38 ± 9%, 31 ± 8%), consistent with a diffusion-limited interpretation in which oxygen availability is likely to influence burning rate [17,18,24]. Open shapes' larger exposed surface area promoted sustained combustion; closed shapes experienced premature extinction through oxygen depletion within the enclosed geometry despite the highest instantaneous mass-loss rates.

Effective buoyancy enhancement factors were: open 1.18 ± 0.07, semi-open 1.24 ± 0.09, closed 1.15 ± 0.06, consistent with DNS predictions ($F_{buoy} = 1.12$–1.28, $Ri \approx 0.8$–1.5) from Sardoy et al. [18]. The semi-open category achieved maximum enhancement, likely through a favourable balance between oxygen flux and retention of hot combustion gases—neither oxygen-starved (as in closed shapes) nor rapidly dispersing (as in fully open shapes).

3.4. Rotational dynamics and aerodynamic properties

Open firebrands showed a mean rotation frequency of 0.58 ± 0.12 Hz (0.85 ± 0.18 spins m^{-1}). Semi-open firebrands rotated faster (0.74 ± 0.16 Hz, 1.03 ± 0.23 spins m^{-1}), suggesting stronger aerodynamic excitation associated with intermediate curvature. Closed shapes reached 0.66 ± 0.11 Hz (1.03 ± 0.19 spins m^{-1}) with relatively predictable motion from symmetric cylindrical geometry (Table 3). The trajectory deviation σ is defined as the standard deviation of lateral (horizontal) position about the

running-mean of the vertical trajectory, evaluated over the quasi-steady 21s observation window; larger σ indicates greater lateral scatter.

Table 3. Rotational dynamics and aerodynamic properties. σ is the trajectory-deviation defined in the text.

Morphology	I (×10^{-6} kg m^2)	Rot. (Hz)	σ (cm)	Edge-on (%)	C_D
Open	2.41 ± 0.64	0.58 ± 0.12	2.3	73	0.68 ± 0.15
Semi-open	3.10 ± 0.89	0.74 ± 0.16	4.1	45	1.23 ± 0.28
Closed	4.04 ± 1.12	0.66 ± 0.11	3.2	58	1.47 ± 0.21

Frame-by-frame orientation analysis—requiring consistent segmentation across all 250,000+ frames—revealed that open shapes maintained preferred edge-on orientations for 73% of flight time versus 45% (semi-open) and 58% (closed). This orientation preference is consistent with a gyroscopic stabilisation mechanism, whereby angular momentum from spin resists aerodynamic tumbling torques. However, the present measurements do not conclusively distinguish gyroscopic stabilisation from passive aerodynamic alignment, in which a flat-plate geometry naturally adopts a minimum-drag orientation through weathercock-like restoring moments. Definitive identification would require time-resolved angular-acceleration measurements or direct torque analysis, beyond the present imaging configuration.

Steady-flight force balance yielded morphology-specific drag coefficients: C_D = 0.68 ± 0.15 (open; consistent with 0.5–0.8 for edge-on flat plates [19,23]); 1.23 ± 0.28 (semi-open); 1.47 ± 0.21 (closed; consistent with broadside-cylinder values 1.0–1.5 [20]).

4. Discussion

4.1. Gyroscopic stabilisation and optimal morphology

The results reveal a correlation linking morphology, rotational dynamics and transport efficiency consistent with rotation-mediated stabilisation, though the data are consistent with — but cannot conclusively distinguish — gyroscopic stabilisation from passive aerodynamic alignment. Low moment of inertia (2.41 × 10^{-6} kg m^2) in open shapes enables rapid spin-up to a moderate rotation frequency (0.58 Hz), providing angular momentum that resists tumbling. The hypothesised gyroscopic moment M_g = Iω × Ω (with Ω the precession rate induced by aerodynamic torques) would maintain edge-on orientation for 73% of flight time, sustaining the lowest measured C_D (0.68). Agreement with Himoto and Tanaka [19] (0.5–0.8 for edge-on plates) supports interpretation of open firebrands as thin plates maintaining a stable low-drag attitude. Alternatively, the flat-plate geometry may adopt an edge-on orientation via weathercock restoring moments without gyroscopic effects; distinguishing the two requires dedicated angular-acceleration measurements.

Trajectory-deviation data provide independent evidence of a stabilisation effect regardless of mechanism: σ = 2.3 cm (open) versus 4.1 cm (semi-open) is a 44% reduction in lateral scatter attributable to orientation stability. Semi-open shapes have the highest rotation frequency (0.74 Hz) and thus the greatest angular momentum per inertia, yet worst trajectory stability—because intermediate curvature produces aerodynamic instabilities driving large-amplitude orientation changes. The high rotation frequency reflects forced response to turbulent excitation, not beneficial stabilisation. This distinction between stabilising and destabilising rotation has not been previously quantified for naturally shaped firebrands, though mechanistic interpretation remains to be established by dedicated experiments. The data therefore show that rotation frequency alone is not a proxy for flight stability; the stabilising effect depends on whether rotation is accompanied by persistent low-drag orientation.

Closed shapes achieve intermediate deviation (σ = 3.2 cm) through geometric symmetry enforcing broadside-to-flow orientations, but at the highest drag (C_D = 1.47), consistent with Lee and Hellman [20]. Since $v_t \propto C_D^{-1/2}$, the 2.2× drag ratio between open and closed shapes produces substantially greater lofting for open morphologies, explaining why open shapes achieved the highest absolute transport heights (136.4 cm under burning + vortex) despite closed shapes showing the greatest relative distance improvement (60%).

4.2. Relative contributions of vortex and combustion

A central quantitative result is the disaggregation of transport enhancement into vortex- and combustion-driven components. Near-identical path distances for vortex-only (22.94 m) and burning + vortex (23.42 m) show that vortical flow modification accounts for ≈41% of the total 44% enhancement relative to control, with combustion adding ≈2% in path-integrated distance. That plume updraft is the primary lofting driver—rather than self-buoyancy of individual firebrands—is not in itself a new finding; it is consistent with wind-tunnel work by Tohidi and Kaye [8] and numerical simulations by Wadhwani et al. [25]. The contribution here is a morphology-resolved, quantitative partition on a single, internally consistent factorial dataset.

The aggregate 2% masks morphology-dependent variation. Three synergistic combustion mechanisms contribute with varying effectiveness. First,

continuous mass loss (31–42% over burning duration) reduces terminal velocity; under the quasi-steady force-balance approximation, semi-open shapes losing 38% mass over 9.7 s show a ≈21% decrease in terminal velocity as gravitational force decreases while aerodynamic form remains relatively constant. Second, hot-gas generation produces localised density reductions, augmenting buoyancy by 13-19% of the initial weight; closed-shape gas retention amplifies this despite shorter burning. Third, preferential consumption of protruding features may evolve the aerodynamic shape in flight, not directly characterised here.

Effective buoyancy enhancement factor variation (F_{buoy} = 1.15–1.24) reflects this interplay. Semi-open shapes achieve maximum enhancement (1.24) via balanced oxygen access and gas retention. Open shapes, despite longer burning and greater total mass consumption, produce lower enhancement (1.18) because high oxygen access disperses buoyant gases before they contribute fully to lofting. These findings suggest that firebrand transport models using morphology-independent combustion effects [21,22] may systematically misrepresent transport for specific bark types.

4.3. Machine learning as an enabling tool for combustion science

Several findings were accessible only because automated tracking provides capabilities qualitatively different from manual methods. Rotational-dynamics and orientation statistics required frame-by-frame analysis across 250,000+ frames—the 73% edge-on statistic for open shapes cannot be obtained from a small number of trajectories. The drag-coefficient determination relies on per-frame segmentation masks providing instantaneous projected area, not just centroid position. The detection of temporary vortex-induced destabilisation of open shapes (124.9 → 119.2 cm) required 12 replicates per condition to resolve significance. The modest mAP reduction during active burning (93.8% vs 95.2%) with a uniform 3.7% interpolation fraction across morphologies (3.5–3.9%) confirms no morphology-dependent bias; ML improves both throughput and objectivity [13].

4.4. Implications for spotting-distance prediction and model relevance

In field conditions, absolute distance determines whether a firebrand reaches an ignitable fuel bed. Open bark strips achieving 24.3 m under burning + vortex conditions, sustained by orientation stability and low drag, remain the dominant spotting hazard, and species producing predominantly open bark morphologies may warrant particular attention in future fuel-hazard assessments near the wildland–urban interface. The present results should not be read as direct predictions of field spotting distance—which additionally depends on ejection height, plume structure, crossflow, thermal state, residual fuel, fragmentation and landing-bed ignitability—but as morphology-specific drag, orientation and combustion-modification parameters for future model development. Dynamical similarity supports restricted parameter translation: laboratory Reynolds (10^3–10^4) and Froude (0.15–0.45) numbers overlap with field values, with drag coefficients varying by <15% across this range [19,20]. The measured C_D (0.68–1.47) and F_{buoy} (1.15–1.24) are suitable for integration into Albini-type spread models [21,22], replacing generic spherical-particle assumptions, pending field validation via instrumented prescribed burns.

5. Conclusions

The YOLOv8n-seg framework (95.9% mAP@0.5 at 70 fps) enabled a 108-experiment factorial investigation resolving combustion physics inaccessible to manual methods. Vortical flow modification is the dominant transport-enhancement mechanism (≈41% increase in path distance over control), with active combustion adding ≈2% through mass loss, buoyancy augmentation (F_{buoy} = 1.15–1.24) and aerodynamic shape evolution. Open firebrands achieve optimal transport through orientation stability—consistent with a hypothesised gyroscopic stabilisation mechanism—where moderate spin rates (0.58 Hz) maintain edge-on orientation for 73% of flight time, yielding the lowest C_D (0.68 ± 0.15) and greatest absolute distances. Morphology-dependent drag coefficients (0.68–1.47) and effective buoyancy enhancement factors (1.15–1.24) provide experimentally constrained parameters for future spotting-model development, pending validation across additional species and field-scale conditions. Limitations include the single-species scope (*Eucalyptus mannifera*), near-wall effects on ≈15% of trajectories, absence of direct torque or angular-acceleration measurements, and lack of in-flight fragmentation characterisation.

CRediT authorship contribution statement

HYLW: Conceptualisation, Methodology, Investigation, Formal analysis, Writing. **ALS:** Conceptualisation, Investigation, Writing. **YZ:** Conceptualisation, Supervision, Resources, Writing.

Declaration of competing interest

The authors declare no competing interests.

Acknowledgements

Supported by the Leverhulme International Fellowship (IAF-2019-034).

References

[1] D.M.J.S. Bowman et al., Vegetation fires in the Anthropocene, Nat. Rev. Earth Environ. 1 (2020) 500–515.

[2] S.L. Manzello (Ed.), Encyclopedia of Wildfires and Wildland-Urban Interface (WUI) Fires, Springer, Cham, 2020.

[3] C.S. Tarifa, P.P. del Notario, F.G. Moreno, On the flight paths and lifetimes of burning particles of wood, Proc. Combust. Inst. 10 (1965) 1021–1037.

[4] P.F. Ellis, The aerodynamic and combustion characteristics of eucalypt bark: a firebrand study, Ph.D. thesis, Australian National University, 2000.

[5] P.F. Ellis, The effect of aerodynamic behaviour of flakes of jarrah and karri bark on their potential behaviour as firebrands, J. R. Soc. West. Aust. 93 (2010) 21–27.

[6] S.L. Manzello, A. Maranghides, W.E. Mell, Firebrand generation from burning vegetation, Int. J. Wildland Fire 16 (2007) 458–462.

[7] S.L. Manzello, S. Suzuki, Generating wind-driven firebrand showers in a laboratory setting, Proc. Combust. Inst. 37 (2019) 3091–3098.

[8] A. Tohidi, N.B. Kaye, Comprehensive wind tunnel experiments of lofting and downwind transport of non-combusting rod-like model firebrands during firebrand shower scenarios, Fire Saf. J. 90 (2017) 95–111.

[9] A. Tohidi, N.B. Kaye, Stochastic modeling of firebrand shower scenarios, Fire Saf. J. 91 (2017) 91–102.

[10] R. Wadhwani, C. Sullivan, A. Wickramasinghe, M. Kyng, N. Khan, K. Moinuddin, A review of firebrand studies on generation and transport, Fire Saf. J. 134 (2022) 103674.

[11] J. Terven, D.M. Córdova-Esparza, J.A. Romero-González, A comprehensive review of YOLO architectures in computer vision: From YOLOv1 to YOLOv8 and YOLO-NAS, Mach. Learn. Knowl. Extr. 5 (2023) 1680–1716.

[12] Ultralytics, YOLOv8: State-of-the-art YOLO models, 2023. https://github.com/ultralytics/ultralytics

[13] N. Bouvet, E.D. Link, S.A. Fink, A framework to characterize WUI firebrand shower exposure using 3D particle tracking and machine learning, Int. J. Multiph. Flow 170 (2024) 104651.

[14] I.K. Knight, The design and construction of a vertical wind tunnel for the study of untethered firebrands in flight, Fire Technol. 37 (2001) 87–100.

[15] I.K. Knight, P.F. Ellis, A.L. Sullivan, The CSIRO vertical wind tunnel, CSIRO Forestry and Forest Products Technical Report No. 133, Canberra, 2001.

[16] Z. Zhang, A flexible new technique for camera calibration, IEEE Trans. Pattern Anal. Mach. Intell. 22 (2000) 1330–1334.

[17] E. Koo, P.J. Pagni, D.R. Weise, J.P. Woycheese, Firebrands and spotting ignition in large-scale fires, Int. J. Wildland Fire 19 (2010) 818–843.

[18] N. Sardoy, J.L. Consalvi, B. Porterie, A.C. Fernandez-Pello, Modeling transport and combustion of firebrands from burning trees, Combust. Flame 150 (2007) 151–169.

[19] K. Himoto, T. Tanaka, Transport of disk-shaped firebrands in a turbulent boundary layer, Fire Saf. Sci. 8 (2005) 433–444.

[20] S.L. Lee, J.M. Hellman, Study of firebrand trajectories in a turbulent swirling natural convection plume, Combust. Flame 13 (1969) 645–655.

[21] F.A. Albini, Spot fire distance from burning trees: a predictive model, USDA Forest Service Gen. Tech. Rep. INT-56, 1979.

[22] F.A. Albini, Potential spotting distance from wind-driven surface fires, USDA Forest Service Res. Pap. INT-309, 1983.

[23] A. Tohidi, N.B. Kaye, Aerodynamic characterization of rod-like debris with application to firebrand transport, J. Wind Eng. Ind. Aerodyn. 168 (2017) 297–311.

[24] J.P. Woycheese, P.J. Pagni, Combustion models for wooden brands, in: Proc. 3rd Int. Conf. Fire Research and Engineering, SFPE, 1999, pp. 53–71.

[25] R. Wadhwani, D. Sutherland, A. Ooi, K. Moinuddin, Firebrand transport from a novel firebrand generator: numerical simulation of laboratory experiments, Int. J. Wildland Fire 31 (2022) 846–858.

[26] S. Suzuki, S.L. Manzello, Firebrand production from building components fitted with siding treatments, Fire Saf. J. 80 (2016) 64–70.

[27] M. Abdelaziz, A.L. Sullivan, Comprehensive methodology for tracking burning firebrands in a vertical wind tunnel using multi-view video analysis, Int. J. Wildland Fire 34 (2025) WF25153. https://doi.org/10.1071/WF25153